J. Fluid Mech. (2017), *vol.* 813, *pp.* 127–151.
doi:10.1017/jfm.2016.864

Experimental and numerical investigation of flames stabilised behind rotating cylinders: interaction of flames with a moving wall

P. Xavier[1,†], A. Ghani[1], D. Mejia[1], M. Miguel-Brebion[1], M. Bauerheim[2], L. Selle[1] and T. Poinsot[1]

[1]Institut de Mécanique des Fluides de Toulouse (IMFT) – Université de Toulouse, CNRS-INPT-UPS, 31400 Toulouse, France

[2]CERFACS, CFD Team, 42 avenue Coriolis, 31057 Toulouse, CEDEX 01, France

(Received 2 July 2016; revised 14 December 2016; accepted 14 December 2016; first published online 17 January 2017)

Steady methane/air laminar premixed flames stabilised on a cylindrical bluff body subjected to a continuous rotation are analysed using joint direct numerical simulations (DNS) and experiments. DNS are carried out using a 19 species scheme for methane/air combustion and a lumped model to predict the cylinder temperature. Rotation of the cylinder induces a symmetry breaking of the flow, and leads to two distinct flame branches in the wake of the cylinder. DNS are validated against experiments in terms of flame topologies and velocity fields. DNS are then used to analyse flame structures and thermal effects. The location and structure of the two flames are differently modified by rotation and heat transfer: a superadiabatic flame branch stabilises close to the hot cylinder and burns preheated fresh gases while a subadiabatic branch is quenched over a large zone and anchors far downstream of the cylinder. Local flame structures are shown to be controlled to first order by the local enthalpy defect or excess due to heat transfer between the cylinder and the flow. An analysis of the local wall heat flux around the cylinder shows that, for low rotation speeds, the superadiabatic flame branch contributes to wall heat fluxes that considerably exceed typical values found for classical flame/wall interactions. However, for high rotation speeds, fluxes decrease because the cylinder is surrounded by a layer of burned gases that dilute incoming reactants and shield it from the flame.

Key words: combustion, flames, laminar reacting flows

1. Introduction

The stabilisation of premixed flames in the wake of obstacles is a key phenomenon in the field of combustion. Bluff bodies are commonly used as ‘flame holders’ to create a low-pressure recirculation zone that allows the flame to anchor in a low-speed region (Williams, Hottel & Scurlock 1951; Longwell 1952; Williams & Shipman 1953; Penner & Williams 1957) where incoming fresh gases mix with hot recirculated gases and ignite (Zukoski & Marble 1956; Chen *et al.* 1990; Correa & Gulati 1992; Masri, Barlow & Carter 1994; Smith *et al.* 2007; Nair & Lieuwen 2007).

† Email address for correspondence: pradip.xavier@imft.fr

Various bluff-body geometries can be used: cylinder, triangle, square, closed cone, closed and open V-gutter, plate, etc. (Zukoski & Marble 1955; Ballal & Lefebvre 1979; Sanquer, Bruel & Deshaies 1998). The fundamental mechanisms involved in flame stabilisation are numerous. Heat transfer between flame holders and the flow, low-temperature chemistry and recirculating gases influence the flame root location (where chemical reactions begin) and determine the ability of a flame to be stabilised (Plee & Mellor 1979; Glassman 1996; Shanbhogue, Husain & Lieuwen 1997; Chen *et al.* 1998; Kedia, Altay & Ghoniem 2011; Mejia *et al.* 2015).

Since flame holders are usually obstacles placed in the flow, they also trigger hydrodynamic instabilities that can lead to situations where the flame is 'stabilised' (i.e. anchored on the flame holder) but 'unstable' (i.e. showing strong fluctuations of heat-release rate coupled with the unsteady flow created by the flame holder). One specific example of such instabilities is thermoacoustic modes where fluctuations in heat-release rate lead to self-excited instabilities due to a constructive coupling between acoustics and combustion (Rayleigh 1878; Culick 1988; Candel 2002; Lieuwen & Yang 2005). These instabilities can restrict the range of operating conditions and yield unacceptable pollutant emissions (Rhee, Talbot & Sethian 1995; Huang & Yang 2009; Stohr *et al.* 2012; Kwong, Geraedts & Steinberg 2016). Even if hydrodynamic modes are not the sole driver of thermoacoustic instabilities, their role in these instability loops has been largely documented (Poinsot & Veynante 2011; Lieuwen 2012; Terhaar, Oberleithner & Paschereit 2015). For example, vortex generation behind obstacles is one typical mechanism leading to thermoacoustic activity (Poinsot *et al.* 1987; Ducruix *et al.* 2003; Ghani *et al.* 2015) which has been identified for a very long time (Reynst 1961). Therefore, our capacity to mitigate these hydrodynamic instabilities is of great importance as it could improve flame stabilisation.

One method to suppress or control these hydrodynamic instabilities is to implement an active or passive control to modify the flow field: micro-jets, vibrating/moving parts, plasma or morphing actuators have been reported (Viets, Piatt & Ball 1981; Gelzer & Amitay 2002; Moreau 2007; Dong, Triantafyllou & Karniadakis 2008; Godoy-Diana *et al.* 2009; Cattafesta & Sheplak 2011; Chinaud *et al.* 2014). Controlling flows around objects has been extensively used in the aerodynamic community to reduce drag or to modify the global flow topology (Roshko 1993; Leweke, Provansal & Boyer 1993; Mittal & Balachandar 1995; Cimbala, Nagib & Roskho 1988; Prasad & Williamson 1997).

A canonical example to illustrate these hydrodynamic flow instabilities is a laminar flow around a cylinder ($Re \leqslant 2000$, based on the cylinder diameter). Kelvin–Helmholtz (KH) instabilities develop in shear layers where velocity gradients induce coherent structures whereas Bénard–von Kármán (BVK) instabilities lead to an asymmetric vortex shedding in the wake of the obstacle (Cantwell & Coles 1983; Monkewitz 1988; Plaschko, Berger & Peralta-Fabi 1993; Kelso, Lim & Perry 1996). The transition to observe such instabilities does not depend only on the Reynolds number Re (Rao, Thompson & Hourigan 2016), but also on the blockage ratio determined by the ratio of the cylinder diameter to the width of the flow passage (Sahin & Owens 2004), or the position of the cylinder with respect to walls (Rao *et al.* 2013). One method to cancel the KH or BVK instabilities is to rotate the cylinder along its axis. Rotation can be used for symmetry breaking and wake control. Depending on the rotation rate (defined as the ratio of the cylinder boundary velocity to the incoming velocity), the usual von Kármán vortex street observed for a fixed cylinder can be suppressed (Badr *et al.* 1990; Schumm, Berger & Monkewitz 1994; Modi 1997;

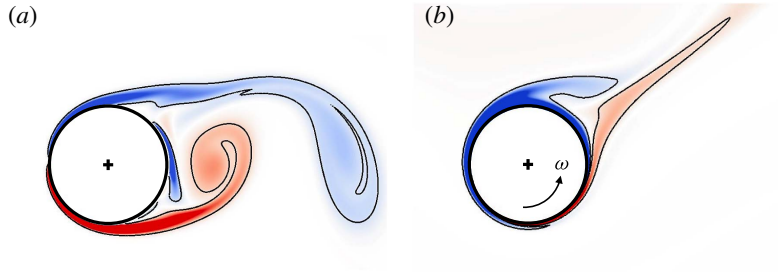

FIGURE 1. (Colour online) Iso-contours of vorticity, coloured by vorticity in the case of a non-reacting flow around (*a*) a non-rotating cylinder and (*b*) a rotating cylinder ($\alpha = 4.10$, α is the rotation rate, see (2.3)).

Coutanceau & Menard 1998; Rao *et al.* 2013; Bourguet & Jacono 2014). An example of the vorticity field obtained by direct numerical simulation (DNS) for a non-rotating and a rotating cylinder (figure 1) shows that rotation can be used to control vortex shedding by creating an asymmetric flow field and when the rotation rate is high enough (figure 1*b*), the vortex street observed for a fixed cylinder totally disappears. Flow control around an obstacle in reactive conditions has received less attention (Mejia *et al.* 2016) and many questions arise regarding flame stabilisation in these conditions.

Therefore, the general aim of the present work is to better understand the stabilisation mechanisms of laminar methane/air premixed flames in the wake of a rotating cylinder. Based on existing non-reacting flow studies, it is expected that rotation will change the flow field, the flame roots location and thus the mean flame topology. Note that this study only deals with steady flames even though the cylinder is rotating. Another goal of this study is that it is a novel technique to create original steady laminar flame structures that differ from the usual laminar premixed flame configurations: planar, cylindrical (Kitano, Kobayashi & Otsuka 1989; Groot & Goey 2002) or spherical (Dowdy, Smith & Taylor 1991; Chen 2011; Bonhomme, Selle & Poinsot 2013).

The specific objectives of the paper are to: (i) analyse the stabilisation of a laminar premixed flame behind a rotating flame holder and compare experimental to numerical results; (ii) analyse the different flame structures in order to understand the key mechanisms leading to the observed flames; and (iii) determine the effects of heat transfer between the flow and the cylinder. This investigation is conducted with both experimental and numerical approaches. The paper first describes the experimental and numerical methods used to study flame stabilised on rotating cylinders (§ 2). Next, flame topologies are presented as a function of the rate of rotation of the cylinder and experimental results are compared to DNS data (§ 3). Third, the structure of each flame branch is analysed using DNS data, taking into account non-adiabadicity in the vicinity of the cylinder: effects of stretch, dilution and cooling will be studied (§ 4). Finally, the distribution of heat transfer on the cylinder wall is studied to examine the interaction between the flame fronts and the rotating cylinder (§ 5).

2. Experimental and numerical methods

2.1. *Experimental set-up*

The experimental set-up consists of a rectangular cross-section combustion chamber ($h = 34$ mm by $l = 94$ mm), operated at atmospheric pressure, in which a stainless

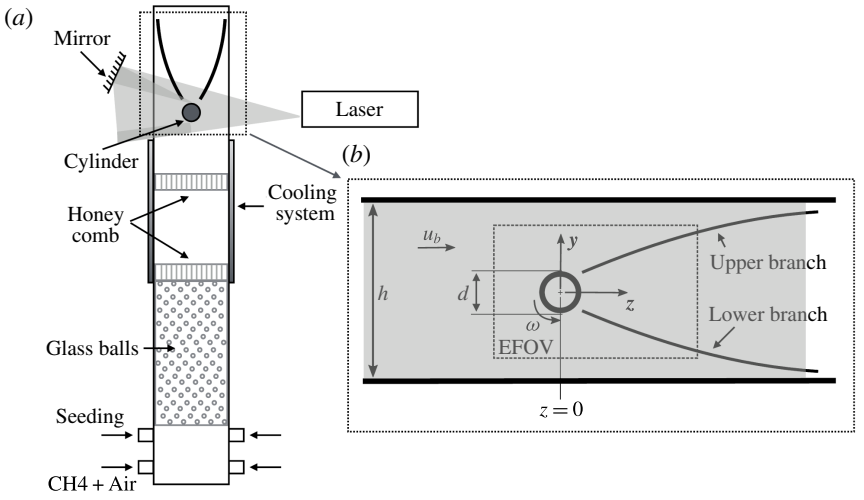

FIGURE 2. (*a*) Schematic of the rotating cylinder in the present configuration. (*b*) Experimental field of view (EFOV) and definition of the controlling parameters. The shaded area corresponds to the computed domain.

steel cylinder with a diameter $d = 8$ mm, serves as the flame holder (figure 2*a*). The cylinder is connected to a brushless direct current electric motor with rotational speed ranging from 600 to 20 000 revolutions per minute (RPM). During experiments, the motor experienced low frequency rotation fluctuations so that the uncertainty on the rotation speed was ± 100 RPM. The flame shape is however weakly sensitive to these fluctuations so that it remains steady. The combustion chamber is equipped with three planar quartz windows allowing optical access. The lean air–methane mixture is injected in a plenum through six injectors. The flow is then laminarised by a bed of 1 mm glass balls and two honeycombs. The upper part of the plenum is water cooled to ensure a constant temperature for the fresh mixture ($T_{in} = 288.15$ K). The velocity field is measured with particle image velocimetry (PIV). A double cavity Nd:YAG laser (Quantel Big Sky), operating at 532 nm, fires two laser beams, with a delay of 200 μs. The laser beam is expanded through a set of fused silica lenses (spherical and diverging). Since the flow is not symmetric when the cylinder is rotating, a tilted mirror is inserted to lighten the cylinder shadow region with a reflection of the incoming laser sheet (figure 2*a*). The laser sheet thickness is measured to 500 μm. Olive oil particles of 1 μm are seeded through two injection systems located just before the glass balls bed (venturi seeder). Mie scattering is collected on a Imager Intense camera (Lavision), operating at a repetition rate of 1 Hz and a resolution of 1376 × 1040 pixels. A f/16 182 mm telecentric lens (TC4M64, Opto-engineering) is used to reduce parallax displacements occurring with classical lenses and obtain more accurate velocity vector fields in the vicinity of the cylinder. A narrow band-pass optical filter, centred at $\lambda_c = 532 \pm 10$ nm is inserted in front of the camera sensor to record only Mie scattering of olive oil particles. PIV images are processed with a cross-correlation multi-pass algorithm (Davis 8.2.3), resulting in a final window of 16 × 16 pix^2 and a 50 % overlap. Ninety images are collected for each operating condition, with a spatial vector spacing of 0.2 mm.

The flame is also visualised thanks to a second Imager Intense camera (Lavision), equipped with a similar telecentric lens as the PIV system. The exposure time is set

to 500 ms and a band-pass optical filter, centred at $\lambda_c = 430 \pm 10$ nm, is placed in front of the camera to record spontaneous CH^* emission.

A 50/50 beam splitter is inserted between the two cameras to simultaneously record PIV and CH^* signals, with only one optical access for visualisation. The experimental field of view (EFOV) shown in figure 2(*b*) captures a part of the combustion chamber section (36 mm $\times$ 26 mm) and the origin is taken at the centre of the cylinder.

The inlet temperature of fresh gases T_{in} and the ambient pressure P_0 are systematically checked prior to measurements, and images are recorded when thermal equilibrium of the combustion chamber is reached (measured with a K-thermocouple fixed on the burner structure). During experiments, the flame started to slightly flicker for certain operating conditions (pressure fluctuations less than 2 Pa). These effects contribute to the slight flame thickening observed in the experiments.

2.2. *Direct numerical simulations*

The reactive multi-species Navier–Stokes equations are solved using a fully compressible unstructured solver called AVBP (Schonfeld & Rudgyard 1999; Moureau *et al.* 2005). A major advantage of the configuration of figure 2 is that it is almost perfectly two-dimensional so that a two-dimensional DNS with detailed chemistry can be used. Chemical kinetics are described by the 'Lu 19' analytical mechanism of Lu & Law (2008) for methane/air combustion. This mechanism involves 19 transported species and 11 quasi-steady state (QSS) species. The viscosity is modelled with a power law, each species has its own Lewis number and a constant Prandtl number is assumed. It was validated for a large range of equivalence ratio ($\phi = 0.5$–1.5), pressure ($P_0 = 1$–30 atm) and correctly predicts auto-ignition times as well as CO levels. It was implemented in the DNS code and validated by comparison with GRI-MECH3.0 computations using the Cantera open source solver (Smith *et al.* 1999; Goodwin 2002). Laminar flame speeds and adiabatic temperatures are correctly reproduced (figure 3*b*). In addition, properties of flame/wall interactions were validated by running one-dimensional flames. For the canonical head-on quenching scenario, the maximum normalised wall heat flux is 0.35 and the corresponding Peclet number is 3, being in agreement with the literature (Huang, Vosen & Greif 1988; Jarosinski 1988; Wichman & Bruneaux 1995). The laminar flame thickness for the $\phi = 0.7$ equivalence ratio flame studied here is 0.680 mm while the mesh resolution in the flame zone is 0.06 mm so that at least 12 points are used to resolve the flame front. Mesh sensitivity was verified by testing a finer mesh, with a cell resolution of 25 μm (instead of 60 μm in this study), leading to negligible modifications in flame position and velocity field.

The two-step Taylor–Galerkin convection scheme (Colin & Rudgyard 2000) used for DNS provides third-order accuracy in time and space. This scheme is characterised by a high spectral resolution, excellent dispersion and dissipation properties. Navier–Stokes characteristic boundary conditions (NSCBC) (Poinsot & Lele 1992; Moureau *et al.* 2005) are applied at inlet and outlet. Lateral walls were modelled as no-slip and isothermal ($T_w = 288$ K). In order to account for the rotation of the cylinder, the velocity of its wall is set at $u_\theta = \omega/2$ in the frame of the burner, where ω is the angular rotation speed. The temperature T_c is imposed at the cylinder external face (see § 2.2.1). The computational domain extends from $z = -35$ to $z = 45$ mm, which corresponds to the shaded zone in figure 2(*b*). The velocity profile at the inlet (figure 3*a*) is imposed by fitting experimental velocity data.

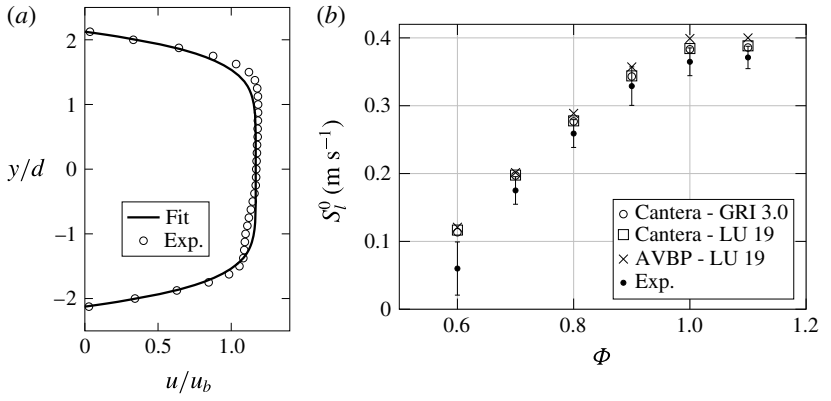

FIGURE 3. (*a*) Experimental inlet velocity profile (hot-wire anemometry) measured at $z/d = -4.6$ and fit used in the simulation (figure 2*a*). (*b*) Laminar burning velocities for air–methane mixtures. Comparison between different solvers, chemical schemes and the experiment of Varea *et al.* (2012).

2.2.1. *Cylinder temperature*

Many recent studies emphasise the importance of the flame holder temperatures on the flame structure and dynamics (Duchaine *et al.* 2011; Kedia & Ghoniem 2013, 2015; Miguel-Brebion *et al.* 2016). The temperature of the flame holder modifies the quenching distance which is the minimum distance between flame front and wall. This distance then controls the flame dynamics so that an accurate DNS of this flame requires a precise determination of the cylinder temperature. This does not necessarily require a full coupled simulation of heat transfer between the cylinder and the flow. An estimation of the Biot number Bi is 0.01, so that very small temperature gradients are expected in the cylinder. Moreover, a one-dimensional model of the wall temperature, considering a periodic and unsteady wall heat flux (related to the rotation speed) gives penetration depths of around 1 mm with negligible temperature fluctuations in the bluff body itself. This proves that the cylinder responds to an average heat flux and thus its temperature is constant when steady state is reached. The temperature within the cylinder can be assumed to be homogeneous and constant so that a simplified lumped model is used to evaluate its temperature, starting from the unsteady heat equation, integrated over the cylinder:

$$\rho C_p V \frac{\mathrm{d}T_c}{\mathrm{d}t} = \int_S \boldsymbol{q} \cdot \boldsymbol{n} \, \mathrm{d}S, \tag{2.1}$$

where T_c is the cylinder temperature, S is its surface, V its volume and $\boldsymbol{q}$ the energy flux at the fluid–solid interface. Thus the cylinder temperature T_c is:

$$\frac{\mathrm{d}T_c}{\mathrm{d}t} = \frac{S}{\rho C_p V}(\Phi_{cond} - \Phi_{rad}), \tag{2.2}$$

where radiative Φ_{rad} and convective Φ_{cond} fluxes are considered at the cylinder boundary. The radiative flux $\Phi_{rad} = \sigma\epsilon(T_c^4 - T_{ext}^4)$ is assumed to be absorbed by the combustion chamber walls at temperature $T_{ext} = T_w$. Additionally, gases are considered as transparent and do not radiate to the cylinder. In the present configuration,

α ($\omega r/u_b$)	u_b (m s^{-1}) Bulk velocity	ϕ Equivalence ratio	T_{in} (K) Fresh gas temperature	P_0 (bar) Pressure	T_c (K)
0.00	1.07	0.70	288	0.99	508
1.16	—	—	—	—	707
2.30	—	—	—	—	783
3.07	—	—	—	—	787
4.10	—	—	—	—	773

TABLE 1. Operating conditions investigated in the present study. The last column gives the temperature of the cylinder (T_c) obtained with (2.2).

$S/(\rho C_p V) = 0.003$ m^2 KJ^{-1} and the emissivity of the cylinder is set to $\epsilon = 0.9$, corresponding to an unpolished used surface. Equation (2.2) is solved at run time and provides the value of the equilibrium wall temperature T_c used as boundary condition for the DNS. The value of $S/(\rho C_p V)$ is only relevant for the resolution of the transient evolution of T_c. Since we are only interested in the steady state, in practice this value is increased in order to speed up the transient phase. Depending on the operating conditions, the radiative heat flux accounts from 12 % to 25 % of the total heat flux. Neglecting its contribution would result in incorrect cylinder temperature and wrong flame stabilisation pattern (Miguel-Brebion *et al.* 2016).

2.3. *Operating conditions*

A large range of operating conditions have been tested in order to determine the stability map of the burner. Based on these observations, the bulk velocity taken in the plenum was set to $u_b = 1.07$ m s^{-1} and the equivalence ratio of the air–methane mixture to $\phi = 0.70$. The Reynolds number Re of the incoming flow is 580 (based on the cylinder diameter d). To characterise the rate of rotation of the cylinder, the normalised parameter α is introduced as:

$$\alpha = \frac{\omega d}{2u_b}. \tag{2.3}$$

This parameter compares the radial velocity at the cylinder to the bulk flow velocity u_b, and is the control parameter for non-reactive flows around rotating cylinders. The fresh gas temperature is $T_{in} = 288.15$ K and the outlet pressure $P_0 = 0.99$ bar. In this study, all parameters are kept constant except for α whose variations are reported in table 1 together with the corresponding cylinder temperature.

3. Experimental and numerical results: flame classification

Figure 4 shows the normalised time averaged CH* signal (grey scale) and an iso-contour of the heat-release rate extracted from the DNS (20 % of the maximum, dashed lines) when the flames have reached steady state. Even though CH* traces do not match exactly reaction rate zones, they are a good indicator of the flame position. The flame roots location obtained in the experiments is well reproduced with the DNS. However, some differences on the flame angle are observed for $z/d > 2$. This latter effect is caused by the chemical scheme that overestimates the laminar burning velocity s_l^0 (figure 3*b*), resulting in a slightly wider flame angle. A V-shape

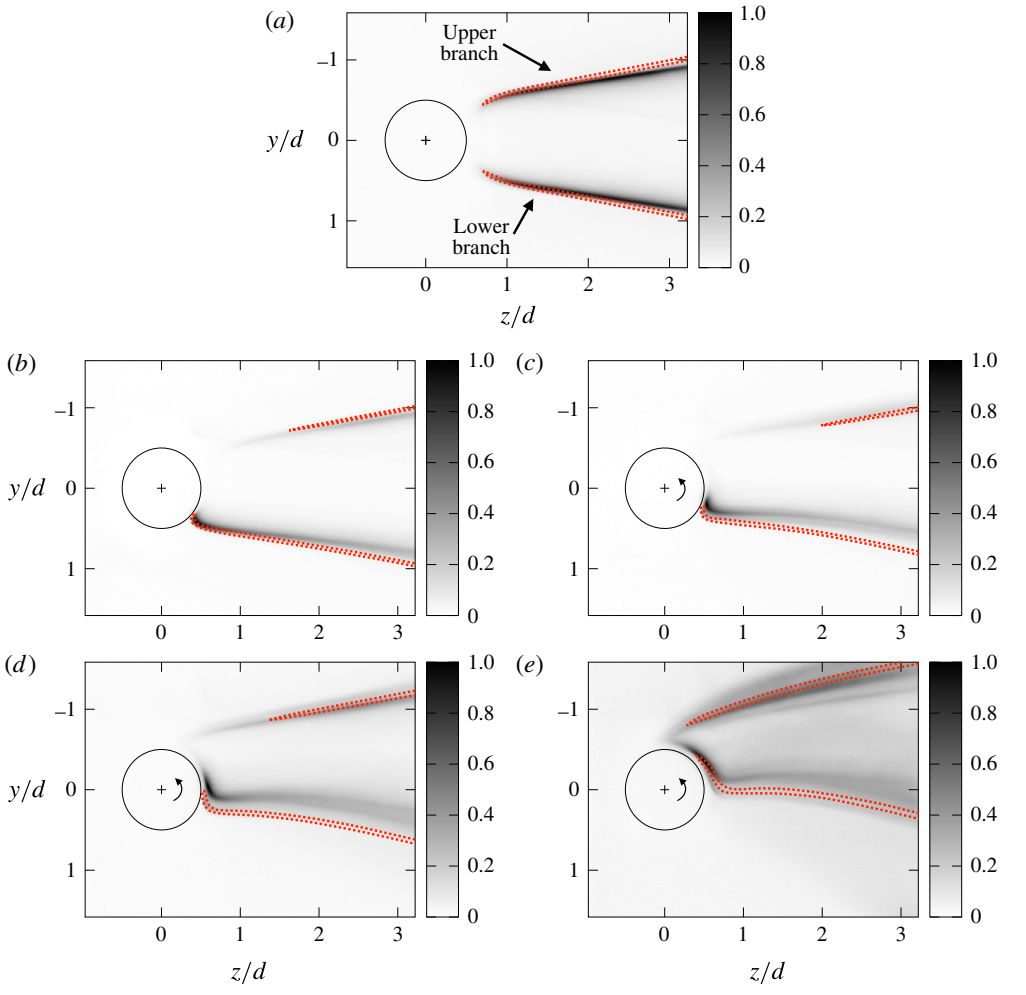

FIGURE 4. (Colour online) Comparison between experimental and DNS flame fronts for increasing rotation rates α. CH* traces from experiments are shown in grey scale and red dashed lines are an iso-contour of the heat release rate from the DNS (20 % of the maximum). (*a*) $\alpha = 0.00$; (*b*) $\alpha = 1.16$; (*c*) $\alpha = 2.30$; (*d*) $\alpha = 3.07$; (*e*) $\alpha = 4.10$. The temperatures of the cylinder are given in table 1.

symmetric flame is observed when there is no rotation, i.e. $\alpha = 0.00$ (figure 4*a*). The flame intensity decreases when approaching the cylinder due to the flame/wall interaction. During the transient period, the cylinder temperature increases due to the presence of burned gases in the wake of the cylinder and flame roots move closer to the cylinder. When thermal equilibrium is reached, the flame roots stabilise at $z/d = 0.66$.

Profiles of axial velocity u (normalised by the bulk velocity upstream of the cylinder, $u_b = 1.07$ m s^{-1}) without rotation ($\alpha = 0$, figure 5, first row) show that the flow speed upstream of the cylinder ($z/d = -0.9$) is affected by the presence of the cylinder. At $z/d = 0.0$, the axial velocity exceeds the bulk velocity u_b by a factor of ≈ 1.7 because of the area restriction (figure 5*b*, top). Negative u values at $z/d = 0.9$ (figure 5*c*, top) reveal a weak symmetric recirculation zone in the wake of the cylinder.

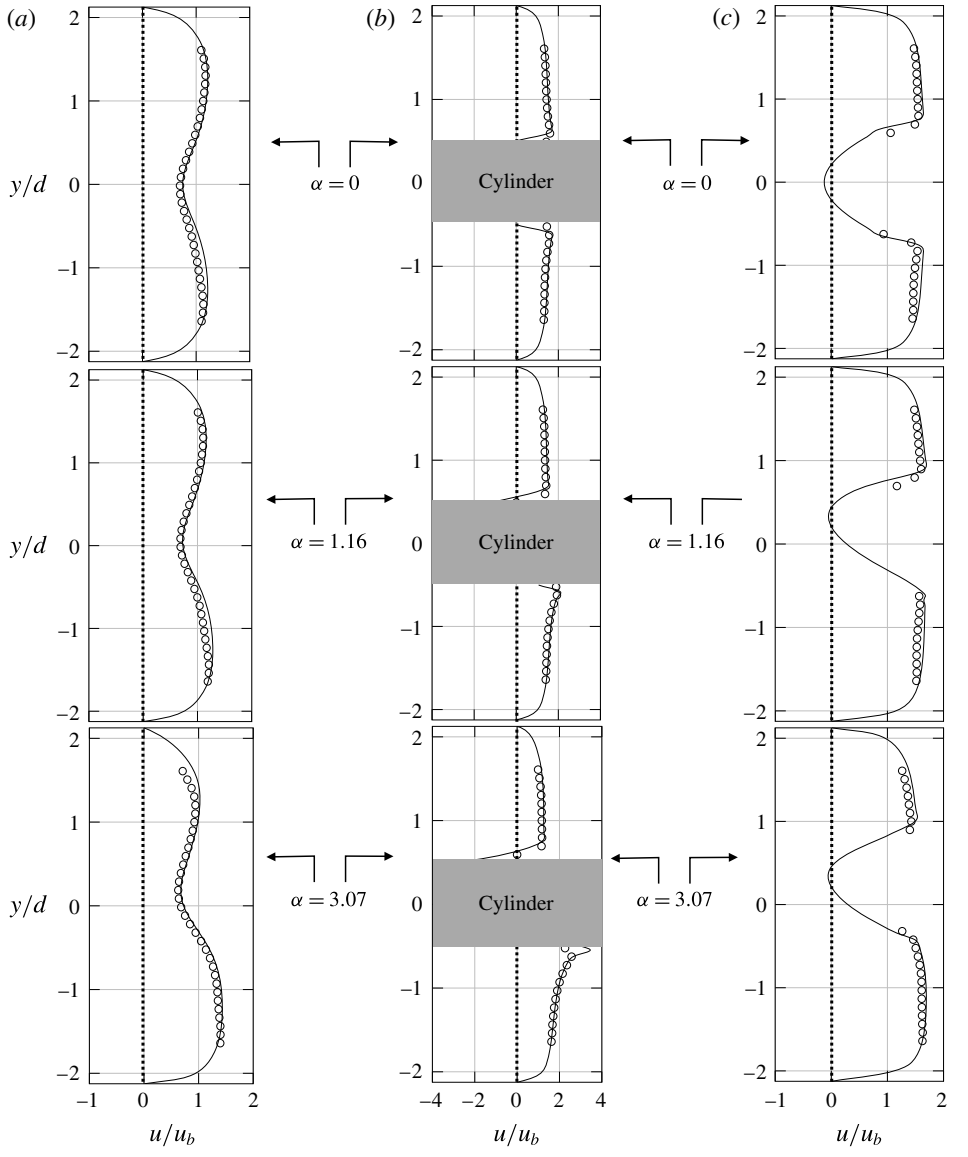

FIGURE 5. Experimental (circles) and DNS (line) mean axial velocity profiles (u/u_b) at three axial locations (columns) and for three different α (rows). The dashed line corresponds to $u/u_b = 0.0$. (*a*) $z/d = -0.9$; (*b*) $z/d = 0.0$; (*c*) $z/d = 0.9$.

When the cylinder has a moderate rotation rate, the flame becomes asymmetric (figure 4*b*: $\alpha = 1.16$ and *c*: $\alpha = 2.30$). Indeed, the lower branch stabilises close to the cylinder and the flame root is more curved when the rotation rate is increased, thus leading to a L-shape flame (figure 4*c*). This branch exhibits a maximum intensity near the cylinder, and decreases along the flame. In contrast, the upper branch is not anchored to the cylinder any more and it is located far downstream of the cylinder. Its intensity is very low and this flame branch is virtually quenched over a large region downstream of the flame holder.

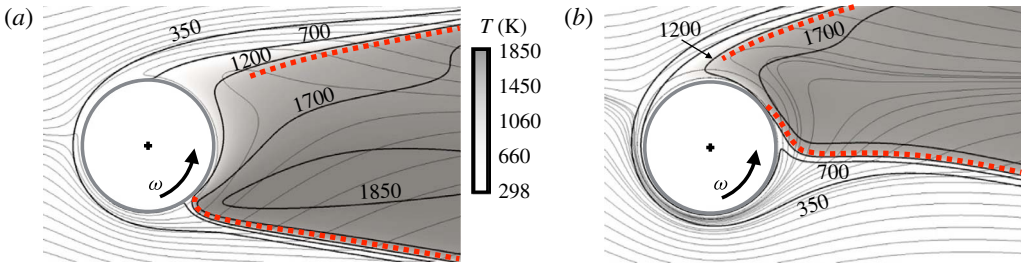

FIGURE 6. (Colour online) Temperature iso-contours (black lines) and flow streamlines (grey lines) for cases: (*a*) $\alpha = 1.16$ and (*b*) $\alpha = 4.10$. The flame location is marked by the heat release crest (red dashed line).

Velocity profiles (figure 5, middle row) show an asymmetric flow at the cylinder and downstream. The cylinder rotation locally increases the flow velocity by a factor of 2, and the recirculation region is affected, being shifted in the direction of the cylinder rotation.

When α is increased to higher values (figure 4*d*: $\alpha = 3.07$ and 4*e*: $\alpha = 4.10$), the lower branch is distorted in the direction of rotation by the high velocities induced by the cylinder. A clear L-shape is observed and the lower flame root location is still close to the cylinder while its intensity remains high. The upper branch is now located closer to the cylinder with higher reactivity, almost leading to an asymmetric U-shape flame.

The velocity profile upstream of the cylinder is affected (figure 5*a* bottom) as it shows a slight asymmetric shape. Finally for larger rotation speeds, the flame topology changes suddenly and it stabilises upstream of the cylinder, a situation which is not discussed in this study. The effect of rotation is visible on the flow streamlines, as shown in figure 6 which displays the flow and temperature fields for $\alpha = 1.16$ and 4.10. For the moderate rotation rate (figure 6*a*), the streamlines are deflected in the direction of the cylinder rotation. When the rotation rate is increased (figure 6*b*), flow streamlines wrap around the cylinder and also shift the temperature iso-contours in the direction of rotation. Moreover, the induced cylinder shear flow may be sufficiently high to continuously carry burned gases to the leading edge of the cylinder.

The five flames of figure 4 exhibit non-trivial stabilisation mechanisms. At moderate rotation rates, the upper branch of the flame is quenched over a long distance so that it is anchored far downstream of the cylinder. In contrast, the lower branch exhibits higher reaction rates in the vicinity of the cylinder (figure 4*b*,*c*).

Figure 7 depicts the different mechanisms involved in this configuration. When the cylinder is rotating, burned gases are carried towards the upper branch while they transfer their energy to heat up the cylinder (Φ_{bg-c}). In parallel, the warm cylinder also heats up the incoming fresh gases (Φ_{c-ug}). As a consequence, the flame roots location and the flame structures are conditioned by heat transfer between the cylinder and the surrounding flow. Moreover, the flow induced by the cylinder rotation mixes fresh and burned gases, and that is dependent on the level of rotation. Figure 8 shows how this mixing affects chemistry. It compares scatter plots of CH_4, CO_2, CH_3 and CO mass fractions versus the progress variable c in two regions of the upper branch: zone A is far away from the cylinder (black dots) whereas region C is located in the quenched zone of the upper flame (grey dots). Flame structures in region A are all similar and collapse on a single curve, showing that, far from the cylinder, there

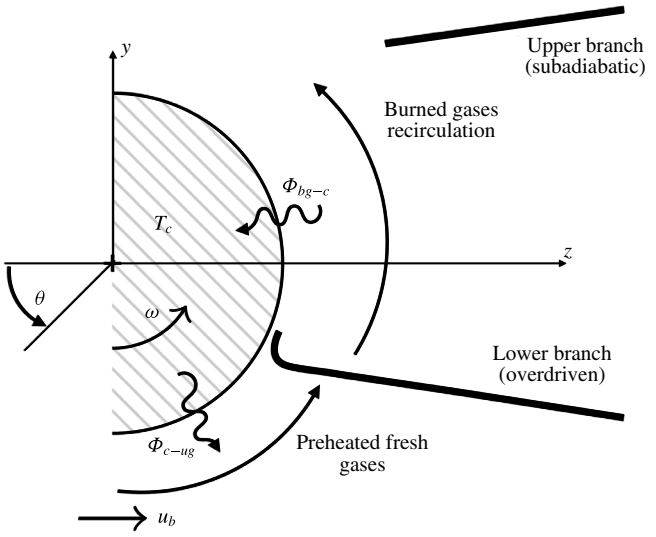

FIGURE 7. Schematic representation of flame stabilisation mechanisms on a rotating cylinder.

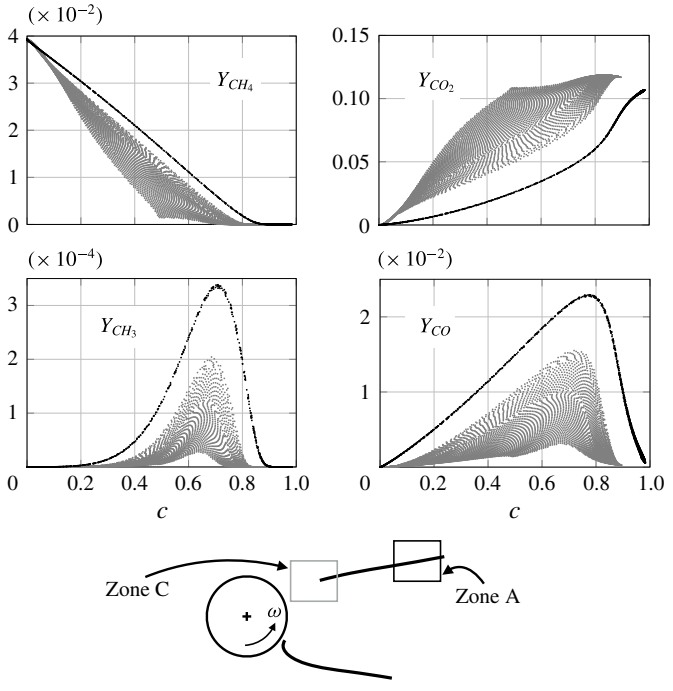

FIGURE 8. Scatter plot of mass fraction Y_k with the progress variable c of different species. Two zones are selected along the upper branch: A (black dots) and C (grey dots). The case corresponds to $\alpha = 1.16$.

is a unique flame structure (which could be tabulated for example). However, the scatter plots in region C reveal multiple flame structures. Burned gases recirculation and subsequent dilution lead to higher CO_2 and lower CH_4 mass fractions. In turn,

formation of radicals and intermediates (CH_3 and CO) is inhibited. In this zone, low-temperature chemistry plays a major role, which is captured by the 'Lu 19' scheme and would not be correctly predicted using tabulation of a global mechanism.

The aim of the next sections is to analyse the two branches of figure 7 in terms of flame structure and flame/wall interaction when the wall (here the cylinder) moves.

4. Analysis of the flame structures

4.1. *Excess or defect of flow enthalpy*

As shown in figure 7, the flow is not adiabatic in the vicinity of the cylinder because of heat transfer with the flame holder. The proper quantity to measure the departure from adiabadicity is the reduced enthalpy defect/excess $\mathcal{L}$ given by:

$$\mathcal{L} = \frac{h_t - h_t^{in}}{QY_F^{in}}, \tag{4.1}$$

where h_t is the total chemical enthalpy taking into account sensible, chemical and kinetic energies. h_t^{in} is a reference enthalpy, taken in the fresh gases. The normalizing term QY_F^{in} in (4.1) is the heat of the reaction. Positive values of $\mathcal{L}$ correspond to sensible or chemical energy given to the fresh gases: the flame is therefore superadiabatic. Conversely, negative values of $\mathcal{L}$ correspond to an enthalpy loss and a subadiabatic flame. Figure 9 presents reduced enthalpy fields for different rotation rates α. Far away from the cylinder and the flame fronts, the flow is adiabatic and $\mathcal{L} = 0$. When the cylinder is not rotating ($\alpha = 0$, figure 9*a*), $\mathcal{L}$ is negative in the wake of the cylinder because hot gases loose energy to the cylinder through conductive heat transfer. Conversely, $\mathcal{L}$ is positive upstream of the cylinder because incoming gases are heated by the cylinder. The latter trend is still valid for moderate values of α and even prominent as $\mathcal{L}$ goes up to 0.2. However, this region of reduced enthalpy gain narrows and eventually vanishes for larger rotation rates (figure 9*e*). The distribution of $\mathcal{L}$ around the cylinder is shown in figure 10 (θ is defined in figure 7). When the cylinder is at rest or has a low rotation rate (i.e. $\alpha = 0.00$ or 1.16), $\mathcal{L}$ is negative in the wake of the cylinder where burned gases are located, and it is positive on the upstream part where fresh gases impact the hot cylinder. Increasing the rotation rate reduces $\mathcal{L}$ all along the cylinder so that it is almost negative at all angles for the higher rotation rate ($\alpha = 4.10$). Therefore, it is speculated that the flow induced by the rotation (figure 6) may explain this trend.

4.2. *Dilution effect at high rotation rates*

Figure 11 displays the field of CO_2 mass fraction at $\alpha = 1.16$ (*a*) and $\alpha = 4.10$ (*b*). For $\alpha = 4.10$, CO_2 is found all around the cylinder. This recirculation of burned gases, also observed in figure 6(*b*), changes the local composition by diluting incoming fresh gases and diminish $\mathcal{L}$ to negative values (figure 10).

To separate preheating and dilution effects, $\mathcal{L}$ can be written as:

$$\mathcal{L} = \underbrace{\frac{1}{QY_F^{in}}\left[\int_{T_0}^{T} C_p \,\mathrm{d}T\right]}_{\mathcal{L}_s} + \underbrace{\frac{1}{QY_F^{in}}\left[\sum_k \Delta h^0_{f,k}(Y_k - Y_{in})\right]}_{\mathcal{L}_c} + \underbrace{\frac{1}{2QY_F^{in}}[(u_i^2 - u_i^{in^2})]}_{\mathcal{L}_k}, \tag{4.2}$$

where $\mathcal{L}_s$ measures gas preheating by the cylinder while $\mathcal{L}_c$ measures the effect of dilution and $\mathcal{L}_k$ accounts for the kinetic effect. Because the Mach number is

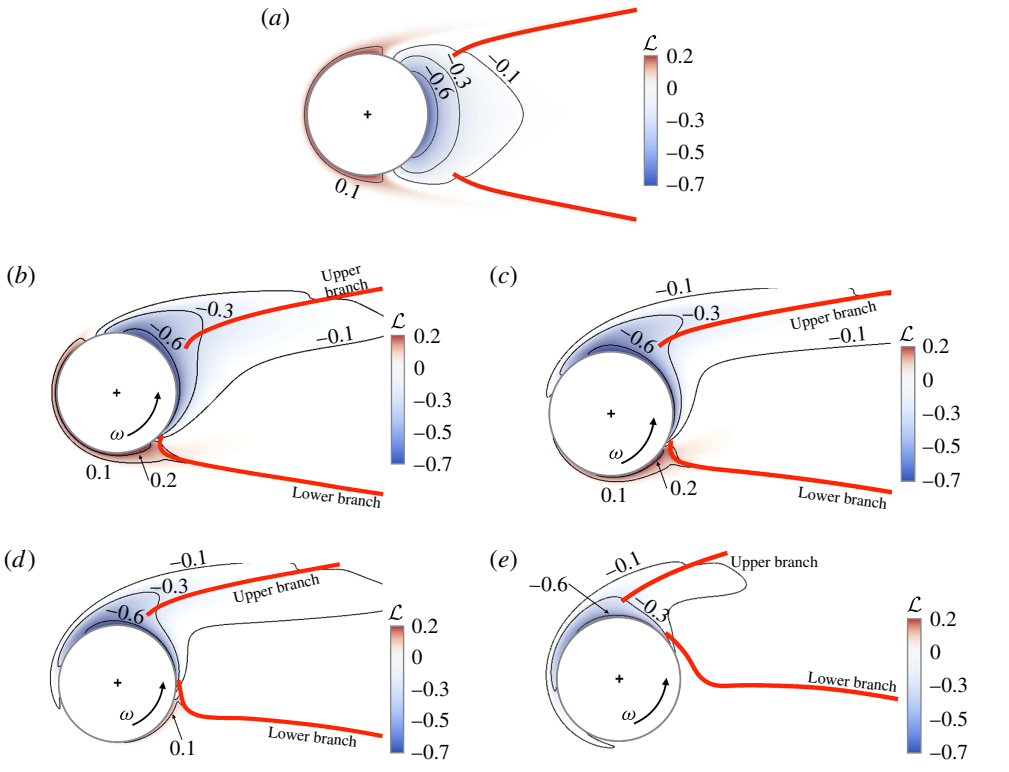

FIGURE 9. (Colour online) Field of enthalpy loss $\mathcal{L}$ for different rotation rates α. Isocontour lines of $\mathcal{L}$ are shown in black. The red thick lines are the heat-release rate crest of each branch. (*a*) $\alpha = 0.00$; (*b*) $\alpha = 1.16$; (*c*) $\alpha = 2.30$; (*d*) $\alpha = 3.07$; (*e*) $\alpha = 4.10$.

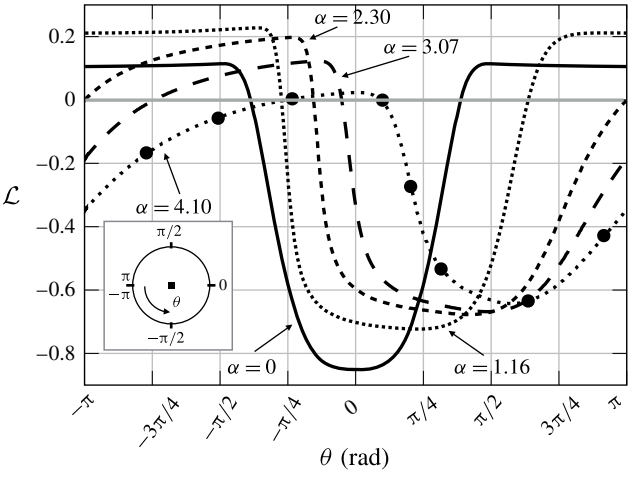

FIGURE 10. Enthalpy loss $\mathcal{L}$ around the cylinder (θ).

0.003, $\mathcal{L}_k$ can be neglected. Figure 12 plots the reduced sensible $\mathcal{L}_s$ (black line) and reduced chemical $\mathcal{L}_c$ enthalpies (dashed line) contributing to $\mathcal{L}$, for two rotation rates $\alpha = 1.16$ (figure 12*a*) and 4.10 (figure 12*b*). The shape or the amplitude of $\mathcal{L}_s$ is

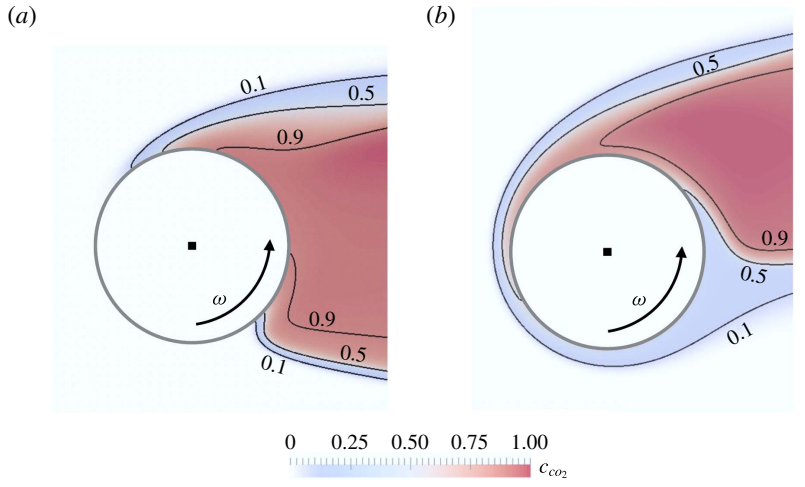

FIGURE 11. (Colour online) Reduced carbon dioxide mass fraction c_{co_2} field for (*a*) $\alpha = 1.16$ and (*b*) $\alpha = 4.10$. Black lines are iso-contour of c_{co_2}.

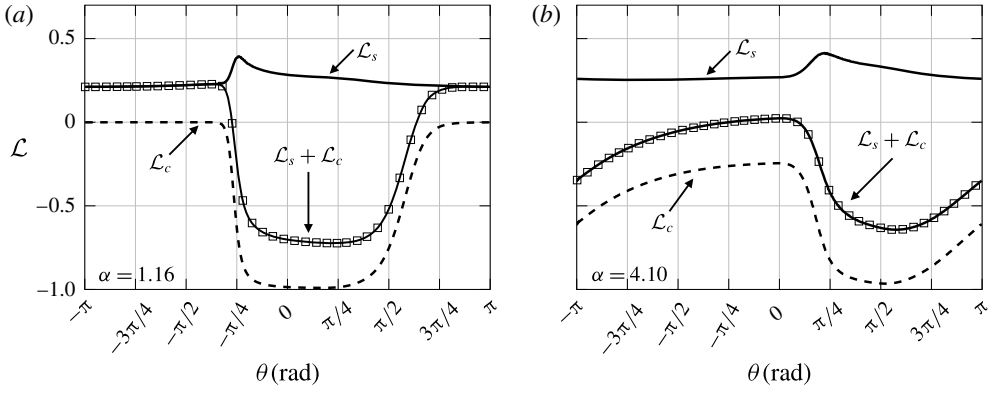

FIGURE 12. Sensible ($\mathcal{L}_s$) and chemical ($\mathcal{L}_c$) enthalpy loss contributions versus position on the cylinder θ. (*a*) $\alpha = 1.16$; (*b*) $\alpha = 4.10$.

similar in both cases because gases near the wall receive energy from the hot cylinder. However, the contribution of $\mathcal{L}_c$ differs from the two cases. At a moderate rotation rate (figure 12*a*), the reduced chemical enthalpy parameter $\mathcal{L}_c$ is null on the upstream part of the cylinder, meaning that only fresh unburned gases are found at this location. In contrast, when the rotation rate is increased (figure 12*b*), $\mathcal{L}_c$ is negative on the leading edge of the cylinder. Therefore, the dilution observed in figure 11(*b*) is the parameter that decreases $\mathcal{L}$ at high rotation rates.

In summary, the excess or defect of the reduced enthalpy $\mathcal{L}$ around the cylinder evolves due to the competition between two effects. First, the warmer cylinder heats up near-wall gases that results in positive values of $\mathcal{L}_s$ for all rotation rates investigated. Second, the induced flow created by the cylinder carries burned gases that diminish the reduced chemical enthalpy $\mathcal{L}_c$. This latter effect is prominent when the rotation rate exceeds a certain threshold ($\alpha_c \approx 3$).

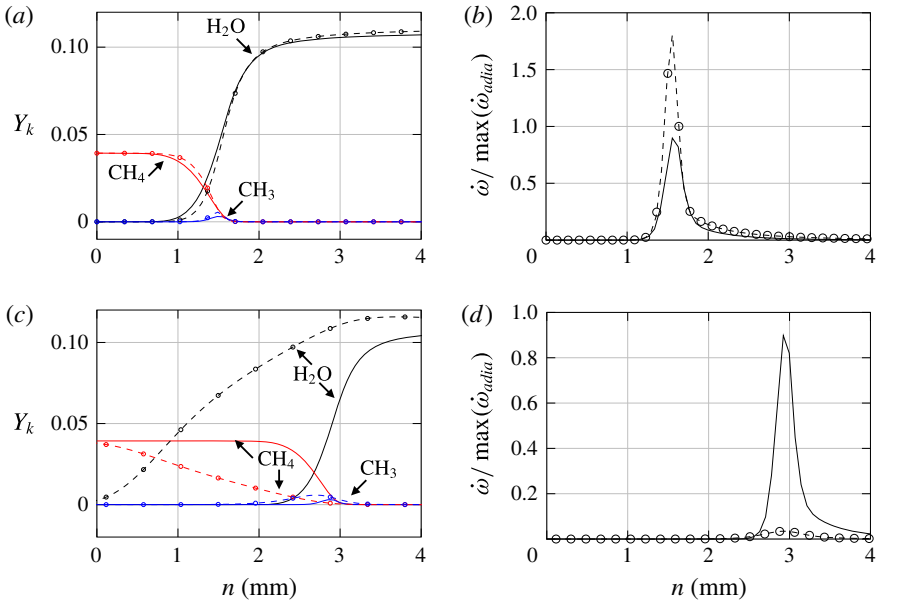

FIGURE 13. (Colour online) Flame profiles extracted from the DNS at $z/d = 1.25$ for the case $\alpha = 1.16$. n is an axis normal to the flame front. Solid lines correspond to an adiabatic unstrained flame. Dashed lines with markers represent the overdriven and cooled branches. (*a*) Species profiles on the overdriven branch. (*b*) Reduced heat-release rate profiles on the overdriven branch. (*c*) Species profiles on the cooled branch. (*d*) Reduced heat-release rate profiles on the cooled branch.

4.3. *Super- and subadiabatic flame structure*

This section focuses on the differences between the two flame branches observed in figure 4 and their link with the reduced enthalpy field (figure 9). Figure 13 shows two flame profiles extracted from the DNS ($\alpha = 1.16$ and $z/d = 1.25$). The comparison between the overdriven lower branch (dashed lines with symbols) and an adiabatic unstrained flame (lines) in figure 13(*a*,*b*) shows a good agreement for the species profiles but the maximum heat-release rate is much higher for the flame of the DNS. This observation is also verified with the reduced enthalpy parameter as this branch is located in a superadiabatic flow ($\mathcal{L} > 0$, figure 13*b*). In contrast, the upper branch (figure 13*c*,*d*) presents smoother species profiles and a heat-release rate profile quite low. Similarly, as the upper branch stabilises in a subadiabatic flow, no self-sustained or weak flame can exist at this location ($\mathcal{L} < 0$, figure 13*d*). Figure 14 presents the evolutions of the maximum heat release rate along the lower flame branch for different rotation rates. The location of maximum heat-release rate is detected with a crest sensor, for both flames and these maximum values are plotted along the curvilinear abscissa s normalised by the flame thickness of a planar unstretched adiabatic flame $\delta_L^0 = (T_b - T_u)/\max(\mathrm{d}T/\mathrm{d}x)$ (0.680 mm for the $\phi = 0.7$ equivalence ratio studied here).

When the cylinder is not rotating (figure 14, solid line), the heat-release rate monotonically increases to reach the value obtained in an adiabatic flame. Close to the cylinder ($s/\delta_L^0 < 10$) the reduced heat-release rate drops, due to the heat losses to the cylinder and the recirculation zones. The zone over which the cylinder inhibits chemical reactions is about $10\delta_l^0$, being larger in comparison to canonical head-on

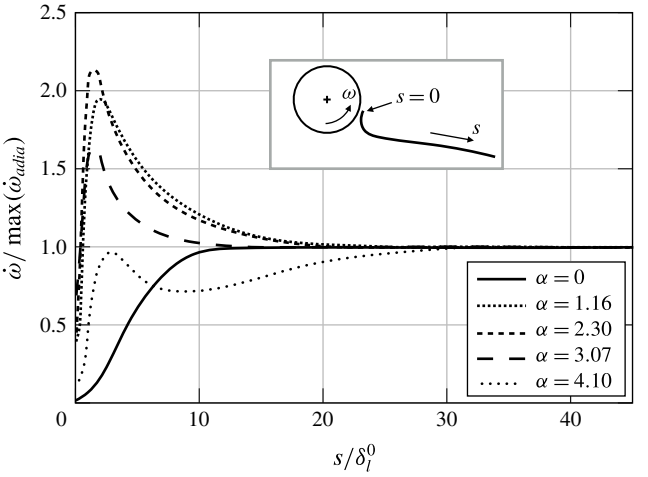

FIGURE 14. Normalised maximum heat-release rate along the lower flame front (overdriven) branch, for rotation rates α from 0.00 to 4.10.

quenching scenarios (Baum *et al.* 1994; Poinsot & Veynante 2011). When the cylinder is rotating at a moderate level ($\alpha = 1.16$, 2.30), the quenching zone narrows to about δ_l^0, and the heat-release rate increases near the wall, being locally twice as intense as in an adiabatic flame. When the rate of rotation is much higher ($\alpha = 3.07$, 4.10), the flame intensity starts to decrease, and it is even lower than in the non-rotating case when $\alpha = 4.10$. This behaviour is an indicator of the dilution effect mentioned previously.

Figure 15 presents the reduced heat-release rate along the upper flame. In contrast with the lower superadiabatic flame branch, all cases exhibit heat-release rates lower than adiabatic conditions. The zone over which the flame is quenched becomes very large. For the case $\alpha = 2.30$, the flame has not recovered its adiabatic structure after $40\delta_l^0$. However, beyond a critical rotation rate ($\alpha_c \approx 3$), as dilution of burned gases shield the cylinder with burned gases, the flame starts to retrieve its adiabatic behaviour.

At this point, $\mathcal{L}$ may be an adequate parameter explaining the flame topologies near the cylinder. In other words, could the two flame structures be explained by considering only local values of $\mathcal{L}$? It is therefore relevant to compute non-adiabatic stretched planar flame with a one-dimensional solver and to compare the local flame structures obtained with DNS flame profiles.

Two different counterflow flame prototypes are considered to mimic the two flame branches only with the reduced enthalpy parameter $\mathcal{L}$. The lower branch corresponds to a superadiabatic flame where fresh gases have been preheated (figure 16*a*) whereas the upper branch corresponds to a flame where fresh gases interact with burned gases that have lost energy to the cylinder (figure 16*b*). However, the computation of a one-dimensional counterflow flame also introduces a strain effect. The range of strain rates to be used for the Cantera computations is evaluated by post-processing the DNS. Figure 17 shows the probability density functions of strain rate κ for the two branches for $\alpha = 0$ to 4.1. For all rotation rates, strain rate values are quite low and the possible mechanism of flame extinction due to an important strain rate is not supported here (Vagelopoulos & Egolfopoulous 1994; Williams 2000; Shanbhogue *et al.* 2016). A small value $\kappa = 300$ s^{-1} is therefore used in the Cantera calculations

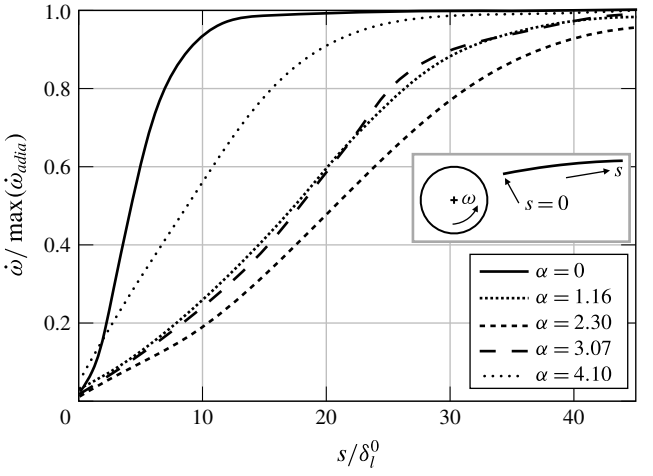

FIGURE 15. Normalised maximum heat-release rate along the curvilinear abscissa of the upper flame (subadiabatic) branch, for various rotation rates α.

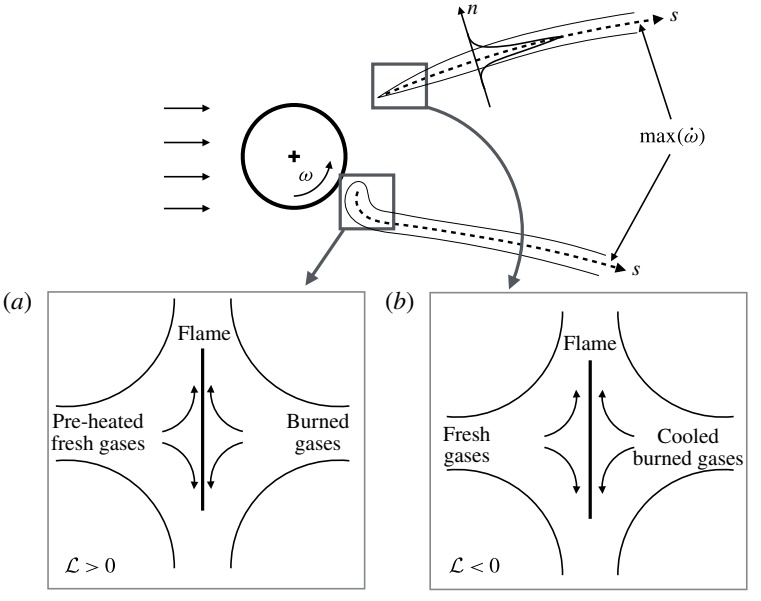

FIGURE 16. Schematic illustration of two Cantera prototypes. (*a*) Overdriven lower branch with preheating; (*b*) cooled upper branch with cold burned gases. Dashed lines mark the heat-release rate crest used to define the curvilinear abscissa s.

and only the reduced enthalpy parameter $\mathcal{L}$ is varied to reproduce the flame structures observed in figures 13–15.

Figures 18 and 19 present plots of the reduced heat-release rate and consumption speed versus the reduced enthalpy $\mathcal{L}$. The consumption speed is evaluated locally by

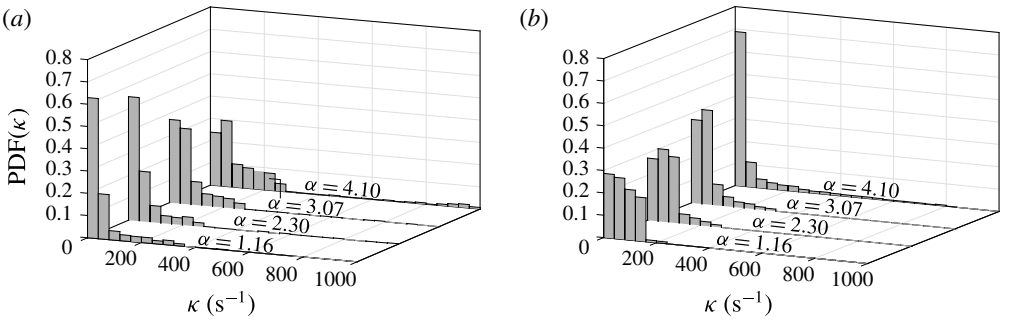

FIGURE 17. Probability density functions of the strain rate κ for different rotation rates. (*a*) Lower branch; (*b*) upper branch.

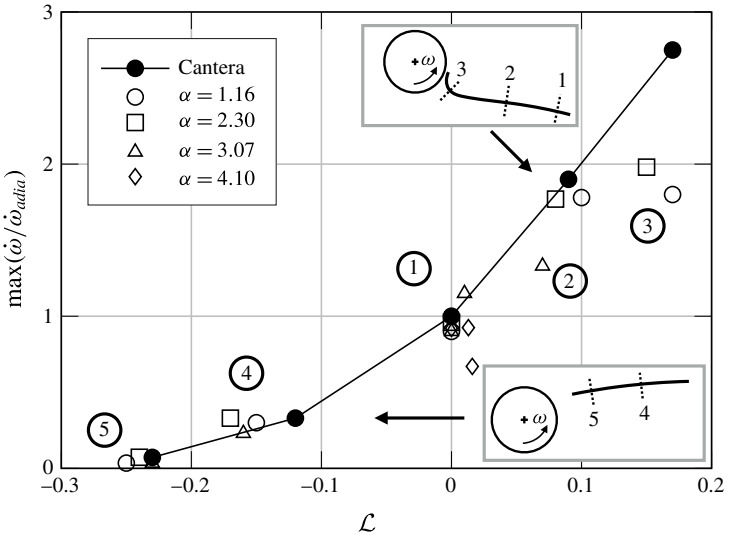

FIGURE 18. Evolution of the reduced maximum heat release $\dot{\omega}/\dot{\omega}_{adia}$ with the enthalpy loss $\mathcal{L}$, and for different rotation rates. The Cantera results (solid black line) are given with the methodology given in figure 16.

integrating the heat release rate on profiles normal to s:

$$S_c = \frac{1}{\rho Y_F^0} \int_{-\infty}^{+\infty} \dot{\omega}_F \, \mathrm{d}n, \tag{4.3}$$

where $\dot{\omega}_F$, ρ and Y_F^0 are the fuel source term, density and fuel mass fraction in the fresh gases, respectively. Data from the DNS have been obtained from profiles taken at $s/\delta_L^0 = 0.7$, 4.7 and 40 for the overdriven branch, and $s/\delta_L^0 = 0.1$, 5.0 and 40 for the cooled branch, and for different rotation rates. The corresponding Cantera results for the two counterflow flame prototypes are shown with the black line. The agreement between the one-dimensional and DNS flame properties is very good, showing that the flame structures observed locally in the DNS can be described to first order by the reduced enthalpy loss parameter $\mathcal{L}$. However, some discrepancies are observed for the lower, superadiabatic branch where curvature effects could modify the flame structure

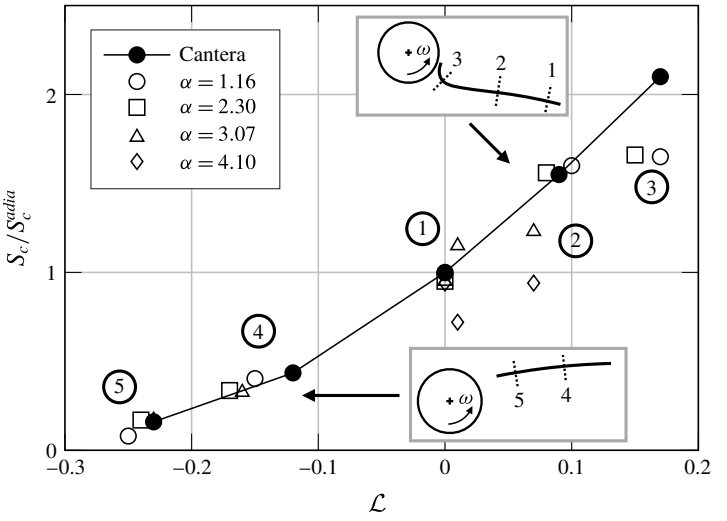

FIGURE 19. Evolution of the reduced consumption speed S_c/S_c^{adia} versus enthalpy loss $\mathcal{L}$, for various rates of rotation. Planar unstretched flames computed with Cantera are plotted for comparison (solid black line).

(label 3). This comparison with one-dimensional flames proves that $\mathcal{L}$ is a robust and adequate parameter to describe the behaviour of the observed flames. Another approach to study this peculiar flame stabilisation is to look at the details of chemical kinetics, as for example done by Michaels & Ghoniem (2016). This analysis for the rotating cylinder is left to a further study.

5. Flame/moving wall interaction

Flame–wall interaction (FWI) is a classical topic in combustion (Ezekoye, Greif & Lee 1992; Poinsot, Haworth & Bruneaux 1993; Wichman & Bruneaux 1995; Bruneaux, Poinsot & Ferziger 1997). In all these studies, the wall is fixed and the main objective is to determine the maximum heat flux it must sustain during FW interaction. Reproducing numerically flame/wall interactions is dependent on the chemical scheme, that needs to mimic the exothermic zero-activation-energy radical recombination, and the chemical reactivity of the wall (Popp, Smooke & Baum 1996; Popp & Baum 1997; Gruber *et al.* 2010; Poinsot & Veynante 2011). The present experiment allows to investigate an interaction between a flame and a moving wall (FMW), which is not the case for classical FWI. For instance, in side wall quenching (SWQ), a flame propagates along a fixed wall (figure 20*b*) and the maximum flux to the wall (scaled by the flame power $\rho s_l^0 Q Y_F$) is of the order of 0.15. In the case of head-on quenching (HOQ) where a flame impinges normal to the wall, It can go up to 0.35 (figure 20*a*) on fixed walls.

Figure 21 presents the reduced wall heat flux F along the cylinder (θ is the angular position), for different rotation rates. All fluxes are scaled by the flame power $\rho s_l^0 Q Y_F$, and the azimuthal locations of the lower and upper flame roots are marked with a circle and a square, respectively. When the cylinder is at rest ($\alpha = 0$), the wall heat flux is symmetric. As the cylinder heats up gases, negative reduced fluxes are found on the upstream part of the cylinder. In contrast, the positive bump in the centre denotes the flux from burned gases to the downstream face of the cylinder. The maximum

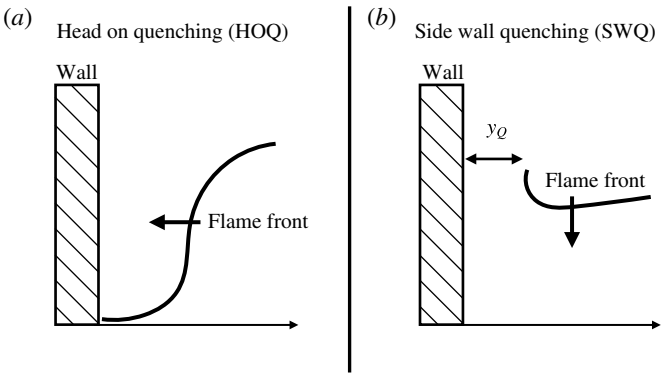

FIGURE 20. Two different types of flame/wall interaction. (*a*) Head-on quenching; (*b*) side wall quenching.

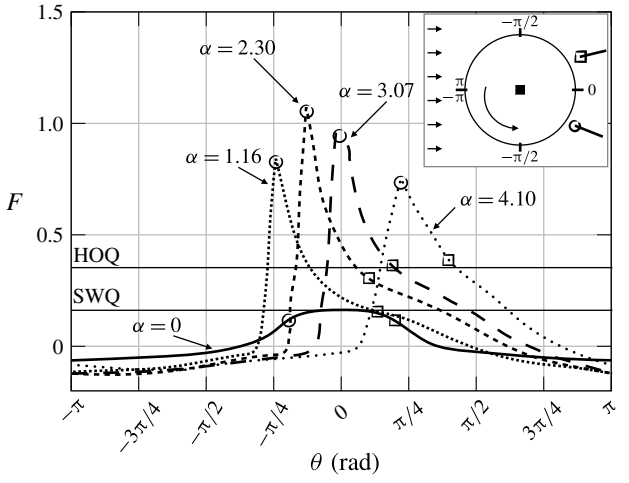

FIGURE 21. Reduced wall heat flux F (scaled by the flame power) along the cylinder, for different rotation rates α. The locations of the lower and upper flame roots are marked with a circle and a square, respectively. The flux is considered as positive when it transfers energy to the cylinder.

reduced wall heat flux is found to be approximately 0.20, which agrees with a typical SWQ flame wall/interaction (Lu *et al.* 1991; Poinsot & Veynante 2011). When the cylinder is rotating with moderate rotation rates ($\alpha = 1.16$ or 2.30), the profile of the wall heat flux becomes asymmetric. A maximum is visible in the vicinity of the lower flame root (circles). The maximum flux obtained at this location reaches a value of 1.1 for $\alpha = 2.30$, which exceeds values for SWQ (0.15) or HOQ (0.35) cases (Wichman & Bruneaux 1995; Poinsot & Veynante 2011). This shows that the flow induced by the rotating cylinder leads to a more intense flame/wall interaction than found in usual flames. It also indicates that the maximum flux which can be reached in a combustion chamber with moving parts (Labarrere *et al.* 2016) can exceed SWQ or HOQ values by almost a factor of three. After the maximum reached at the lower branch location, the local wall heat flux decays in the direction of the cylinder rotation, and the upper

flame root does not create a new local flame maximum as this flame is subadiabatic and stabilises far downstream of the cylinder.

For higher rotation rates ($\alpha > 3$), the maximum heat flux decreases, even if it remains higher than for classical FW interaction. This trend can be explained by the dilution effect seen in figures 10 and 12. The flow induced by the cylinder creates a layer of burned gases that insulate the cylinder from the flame roots. This leads to a thermal shielding and explains that the cylinder temperature T_c does not increase any more (table 1).

6. Conclusion

The stabilisation of a lean premixed laminar methane/air flame on a rotating cylindrical bluff body was investigated with experiments and DNS to obtain more insights on flame stabilisation. All flames studied were steady both in the experiment and in the DNS. Computations were carried out on a two-dimensional grid with an analytically chemical scheme that could accurately capture flame/wall interactions scenarios and low-temperature chemistry in the wake of the cylinder. In addition, a lumped model was implemented to adapt the cylinder temperature with an energy balance coupled to the DNS. An excellent agreement is found between DNS and experiments over a wide range of rotation rates (ratio of the cylinder's surface speed to the incoming cold flow) and results show that the bluff-body rotation breaks the symmetry of the flow and creates two distinct flame branches. Surprisingly, a bifurcation takes place at high rotation rates. Beyond a certain rotation rate, the flow induced by the rotation of the cylinder circulates burned gases all around the cylinder, thus creating a layer of gases that changes locally the gas composition. As a result, it reduces the wall heat flux and the cylinder temperature does not increase any more.

DNS results show that the reduced enthalpy defect/gain $\mathcal{L}$ is an appropriate control parameter to describe the structure of the two branches. Strain remains small and does not contribute to the flame stabilisation. The superadiabatic branch (positive $\mathcal{L}$) burns fresh gases that have been preheated while flowing along the hot cylinder. In contrast, the subadiabatic branch (negative $\mathcal{L}$) interacts with combustion products that have lost their enthalpy while being convected by the flow induced by the cylinder rotation. The local structures of the two branches can be predicted in terms of maximum heat-release rate and consumption speed using planar unstretched non-adiabatic flames (computed with Cantera) and considering only the local value of the reduced enthalpy parameter $\mathcal{L}$.

This study also unveiled a configuration to investigate FMW (flame/moving wall), something that was not studied before. The wall heat fluxes generated by the interaction of the subadiabatic flame with the moving walls of the cylinder are lower than what is observed when a premixed flame hits a wall in head-on (HOQ) or side-wall quenching (SWQ) configurations. However, the superadiabatic flame creates a wall heat flux to the cylinder that exceeds HOQ by a factor of almost three, showing that the interaction between a flame and a moving wall can be very different and more intense than it is in classical HOQ or SWQ situations.

Acknowledgements

The research leading to these results has received funding from the European Research Council under the European Union's Seventh Framework Programme (FP/2007-2013)/ERC Grant Agreement ERC-AdG 319067-INTECOCIS. This work was granted access to the high-performance computing resources of IDRIS under

the allocation x20162b7036 made by Grand Equipement National de Calcul Intensif. Access to the PIV/CH* acquisition system was obtained through the Toulouse Fermat Federation. The CFD team at Cerfacs is acknowledged for its support on the AVBP code.

The authors wish also to thank M. Marchal and S. Cazin from IMFT for their precious help with the experimental diagnostics, and G. Daviller (Cerfacs), C. Lapeyre (IMFT), C. Kraus (IMFT) and B. Bedat (IMFT) for useful discussions.

REFERENCES

BADR, H. M., COUTANCEAU, M., DENNIS, S. C. R. & MENARD, C. 1990 Unsteady flow past a rotating circular cylinder at Reynolds numbers 10^3 and 10^4. *J. Fluid Mech.* **220**, 459–484.

BALLAL, D. R. & LEFEBVRE, A. H. 1979 Weak extinction limits of turbulent flowing mixtures. *Trans. ASME J. Engng Gas Turbines Power* **101**, 343–348.

BAUM, M., POINSOT, T. J., HAWORTH, D. C. & DARABIHA, N. 1994 Progress in knowledge of flamelet structure and extinction. *J. Fluid Mech.* **280**, 1–32.

BONHOMME, A., SELLE, L. & POINSOT, T. 2013 Curvature and confinement effects for flame speed measurements in laminar spherical and cylindrical flames. *Combust. Flame* **160**, 1208–1214.

BOURGUET, R. & JACONO, D. L. 2014 Flow-induced vibrations of a rotating cylinder. *J. Fluid Mech.* **740**, 342–380.

BRUNEAUX, G., POINSOT, T. & FERZIGER, J. H. 1997 Premixed flame wall interaction in a turbulent channel flow: budget for the flame surface density evolution equation and modelling. *J. Fluid Mech.* **349**, 191–219.

CANDEL, S. 2002 Combustion dynamics and control: progress and challenges. *Proc. Combust. Inst.* **29** (1), 1–28.

CANTWELL, B. & COLES, D. 1983 An experimental study of entrainment and transport in the turbulent near wake of a circular cylinder. *J. Fluid Mech.* **136**, 321–374.

CATTAFESTA, L. N. & SHEPLAK, M. 2011 Actuators for active flow control. *Annu. Rev. Fluid Mech.* **43**, 247–272.

CHEN, R. H., DRISCOLL, J. F., KELLY, J., NAMAZIAN, M. & SCHEFER, R. W. 1990 A comparison of bluff-body and swirl-stabilized flames. *Combust. Sci. Technol.* **71**, 197–217.

CHEN, Y. C., CHANG, C. C., PAN, K. L. & YANG, J. T. 1998 Flame lift-off and stabilization mechanisms of nonpremixed jet flames on a bluff-body burner. *Combust. Flame* **115**, 51–65.

CHEN, Z. 2011 On the extraction of laminar flame speed and Markstein length from outwardly propagating spherical flames. *Combust. Flame* **158** (2), 291–300.

CHINAUD, M., ROUCHON, M., DUHAYON, J. F., SCHELLER, J., CAZIN, S., MARCHAL, M. & BRAZA, M. 2014 Trailing-edge dynamics and morphing of a deformable flat plate at high Reynolds number by time-resolved PIV. *J. Fluid Struct.* **47**, 41–54.

CIMBALA, J. M., NAGIB, H. M. & ROSKHO, A. 1988 Large structure in the far wakes of two-dimensional bluff bodies. *J. Fluid Mech.* **190**, 265–298.

COLIN, O. & RUDGYARD, M. 2000 Development of high-order Taylor–Galerkin schemes for unsteady calculations. *J. Comput. Phys.* **162**, 338–371.

CORREA, S. M. & GULATI, A. 1992 Measurements and modeling of a bluff body stabilized flame. *Combust. Flame* **89**, 195–213.

COUTANCEAU, M. & MENARD, C. 1998 Influence of rotation on the near-wake development behind an impulsively started circular cylinder. *J. Fluid Mech.* **158**, 399–446.

CULICK, F. E. C. 1988 Combustion instabilities in liquid-fueled propulsion systems. In *AGARD Conference Proceedings,* no. 450.

DONG, S., TRIANTAFYLLOU, G. S. & KARNIADAKIS, G. E. 2008 Elimination of vortex streets in bluff-body flows. *Phys. Rev. Lett.* **100**, 204501.

DOWDY, D. R., SMITH, D. B., TAYLOR, S. C. & WILLIAMS, A. 1991 The use of expanding spherical flames to determine burning velocities and stretch effects in hydrogen/air mixtures. In *Symp. (Int.) on Combustion*, vol. 23, pp. 325–332. Elsevier.

DUCHAINE, F., BOUDY, F., DUROX, D. & POINSOT, T. 2011 Sensitivity analysis of transfer functions of laminar flames. *Combust. Flame* **158** (12), 2384–2394.

DUCRUIX, S., SCHULLER, T., DUROX, D. & CANDEL, S. 2003 Combustion dynamics and instabilities: elementary coupling and driving mechanisms. *J. Prop. Power* **19**, 722–734.

EZEKOYE, O., GREIF, R. & SAWYER, R. F. 1992 Increased surface temperature effects on wall heat transfer during unsteady flame quenching. In *Symp. (Int.) on Combustion*, vol. 24, pp. 1465–1472. Elsevier.

GELZER, A. & AMITAY, M. 2002 synthetic jets. *Annu. Rev. Fluid Mech.* **34**, 503–529.

GHANI, A., POINSOT, T., GICQUEL, L. & STAFFELBACH, G. 2015 LES of longitudinal and transverse self-excited combustion instabilities in a bluff-body stabilized turbulent premixed flame. *Combust. Flame* **162**, 4075–4083.

GLASSMAN, I. 1996 *Combustion*. Academic.

GODOY-DIANA, R., MARAIS, C., AIDER, J.-L. & WESFREID, J. E. 2009 A model for the symmetry breaking of the reverse Benard von Karman vortex street produced by a flapping foil. *J. Fluid Mech.* **622**, 23–32.

GOODWIN, D. G. 2002. Cantera C++ users guide. *Tech. Rep*. California Institute of Technology.

GROOT, G. R. A. & DE GOEY, L. P. H. 2002 A computational study on propagating spherical and cylindrical premixed flames. *Proc. Combust. Inst.* **29** (2), 1445–1451.

GRUBER, A., SANKARAN, R., HAWKES, E. R. & CHEN, J. H. 2010 Turbulent flame-wall interaction: a direct numercial simulation study. *J. Fluid Mech.* **658**, 5–32.

HUANG, W. M., VOSEN, S. R. & GREIF, R. 1988 Heat transfer during laminar flame quenching: effect of fuels. In *Symp. (Int.) on Combustion*, vol. 21, pp. 1853–1860. Elsevier.

HUANG, Y. & YANG, V. 2009 Dynamics and stability of lean-premixed swirl-stabilized combustion. *Prog. Energy Combust. Sci.* **35**, 293–364.

JAROSINSKI, J. 1988 A survey of recent studies on flame extinction. *Combust. Sci. Technol.* **12**, 88–116.

KEDIA, K. S., ALTAY, H. M. & GHONIEM, A. F. 2011 Impact of flame-wall interaction on premixed flame dynamics and transfer function characteristics. *Proc. Combust. Inst.* **33**, 1113–1120.

KEDIA, S. K. & GHONIEM, A. F. 2013 An analytical model for the prediction of the dynamic response of premixed flames stabilized on a heat-conducting perforated plate. *Proc. Combust. Inst.* **34** (1), 921–928.

KEDIA, S. K. & GHONIEM, A. F. 2015 The blow-off mechanism of a bluff-body stabilized laminar premixed flame. *Combust. Flame* **162** (4), 1304–1315.

KELSO, R., LIM, T. & PERRY, A. 1996 An experimental study of round jets in cross-flow. *J. Fluid Mech.* **306**, 111–144.

KITANO, M., KOBAYASHI, H. & OTSUKA, Y. 1989 A study of cylindrical premixed flames with heat loss. *Combust. Flame* **76**, 89–105.

KWONG, A. Q., GERAEDTS, B. D. & STEINBERG, A. M. 2016 Coupled dynamics of lift-off and precessing vortex core formation in swirl flames. *Combust. Flame* **168**, 228–239.

LABARRERE, L., POINSOT, T., DAUPTAIN, A., DUCHAINE, F., BELLENOUE, M. & BOUST, B. 2016 Experimental and numerical study of cyclic variations in a constant volume combustion chamber. *Combust. Flame* **172**, 49–61.

LEWEKE, T., PROVANSAL, M. & BOYER, L. 1993 Stability of vortex shedding modes in the wake of a ring at low Reynolds numbers. *Phys. Rev. Lett.* **71**, 3469–3473.

LIEUWEN, T. & YANG, V. 2005 Combustion instabilities in gas turbine engines. Operational experience, fundamental mechanisms and modeling. In *Prog. in Astronautics and Aeronautics AIAA*, vol. 210.

LIEUWEN, T. C. 2012 *Unsteady Combustor Physics*. Cambridge University Press.

LONGWELL, J. P. 1952 Flame stabilization by bluff bodies and turbulent flames in ducts. *Proc. Combust. Inst.* **4**, 97–97.

LU, J. H., EZEKOYE, O., GREIF, R. & SAWYER, R. F. 1991 Unsteady heat transfer during side wall quenching of a laminar flame. In *Symp. (Int.) on Combustion*, vol. 23, pp. 441–446. Elsevier.

LU, T. & LAW, C. K. 2008 A criterion based on computational singular perturbation for the identification of quasi steady state species: a reduced mechanism for methane oxidation with no chemistry. *Combust. Flame* **154**, 761–774.

MASRI, A. R., DALLY, B. B., BARLOW, R. S. & CARTER, C. D. 1994 The structure of the recirculation zone of a bluff-body combustor. In *Symp. (Int.) on Combustion*, vol. 25, pp. 1301–1308. Elsevier.

MEJIA, D., BAUERHEIM, M., XAVIER, P., FERRET, B., SELLE, L. & POINSOT, T. 2016 Three-dimensionality in the wake of a rotating cylinder in a uniform flow. *Proc. Combust. Inst.* **717**, 1–29.

MEJIA, D., SELLE, L., BAZILE, R. & POINSOT, T. 2015 Wall-temperature effects on flame response to acoustic oscillations. *Proc. Combust. Inst.* **35**, 3201–3208.

MICHAELS, D. & GHONIEM, A. F. 2016 Impact of the bluff-body material on the flame leading edge structure and flame-flow interaction of premixed CH_4/air flames. *Combust. Flame* **172**, 62–78.

MIGUEL-BREBION, M., MEJIA, D., XAVIER, P., DUCHAINE, F., BEDAT, B., SELLE, L. & POINSOT, T. 2016 Joint experimental and numerical study of the influence of flame holder temperature on the stabilization of a laminar methane flame on a cylinder. *Combust. Flame* **172**, 153–161.

MITTAL, R. & BALACHANDAR, S. 1995 Generation of streamwise vortical structures in bluff body wakes. *Phys. Rev. Lett.* **75**, 1300–1304.

MODI, V. J. 1997 Moving surface boundary-layer control: a review. *J. Fluids Struct.* **11**, 627–663.

MONKEWITZ, P. A. 1988 A note on vortex shedding from axisymmetric bluff bodies. *J. Fluid Mech.* **192**, 561–575.

MOREAU, E. 2007 Airflow control by non-thermal plasma actuators. *J. Phys. D: Appl. Phys.* **40**, 605–636.

MOUREAU, V., LARTIGUE, G., SOMMERER, Y., ANGELBERGER, C., COLIN, C. & POINSOT, T. 2005 Numerical methods for unsteady compressible multi-component reacting flows on fixed and moving grids. *J. Comput. Phys.* **202**, 710–736.

NAIR, S. & LIEUWEN, T. 2007 Near-blowoff dynamics of a bluff-body stabilized flames. *J. Prop. Power* **2**, 421–428.

PENNER, S. S. & WILLIAMS, F. 1957 Recent studies on flame stabilization of premixed turbulent gases. *Appl. Mech. Rev.* **10**, 229–237.

PLASCHKO, P., BERGER, E. & PERALTA-FABI, R. 1993 Periodic flow in the near wake of straight circular cylinders. *Phys. Fluids* **5**, 1718–1725.

PLEE, S. L. & MELLOR, A. M. 1979 Characteristic time correlation for lean blow off of bluffbody stabilized flames. *Combust. Flame* **35**, 61–80.

POINSOT, T. & LELE, S. K. 1992 Boundary conditions for direct simulations of compressible viscous flows. *J. Comput. Phys.* **101**, 104–129.

POINSOT, T. & VEYNANTE, D. 2011 *Theoretical and Numerical Combustion*, 3rd edn. Available at: www.cerfacs.fr/elearning.

POINSOT, T. J., HAWORTH, D. C. & BRUNEAUX, G. 1993 Direct simulation and modeling flame-wall interaction for premixed turbulent combustion. *Combust. Flame* **95**, 118–132.

POINSOT, T. J., TROUVE, A., VEYNANTE, D. P., CANDEL, S. M. & ESPOSITO, E. J. 1987 Vortex-driven acoustically coupled combustion instabilities. *J. Fluid Mech.* **177**, 265–292.

POPP, P. & BAUM, M. 1997 An analysis of wall heat fluxes, reaction mechanisms and unburnt hydrocarbons during the head-on quenching of a laminar flame methane flame. *Combust. Flame* **108**, 327–348.

POPP, P., SMOOKE, M. & BAUM, M. 1996 Heterogeneous/homogeneous reactions and trasport coupling during flame-wall interaction. *Proc. Combust. Inst.* **26**, 2693–2700.

PRASAD, A. & WILLIAMSON, C. H. K. 1997 The instability of the shear layer separating from a bluff body. *J. Fluid Mech.* **333**, 375–402.

RAO, A., LEONTINI, J., THOMPSON, M. C. & HOURIGAN, K. 2013 Three-dimensionality in the wake of a rotating cylinder in a uniform flow. *J. Fluid Mech.* **717**, 1–29.

RAO, A., THOMPSON, M. C. & HOURIGAN, K. 2016 A universal three-dimensional instability of the wakes of two-dimensional bluff bodies. *J. Fluid Mech.* **792**, 50–66.

RAYLEIGH, L. 1878 The explanation of certain acoustic phenomena. *Nature* **18**, 319–321.

REYNST, F. H. 1961 *Pulsating Combustion* (ed. M. Thring), Pergamon.

RHEE, C., TALBOT, L. & SETHIAN, J. 1995 Dynamic behavior of premixed turbulent v-flame. *J. Fluid Mech.* **300**, 87–115.

ROSHKO, A. 1993 Perspectives on bluff body aerodynamics. *J. Wind Engng Ind. Aerodyn.* **49**, 79–100.

SAHIN, M. & OWENS, R. G. 2004 A numerical investigation of wall effects up to high blockage ratios on two-dimensional flow past a confined circular cylinder. *Phys. Fluids* **16**, 1305–1320.

SANQUER, S., BRUEL, P. & DESHAIES, B. 1998 Some specific characteristics of turbulence in the reactive wakes of bluff bodies. *AIAA J.* **6**, 994–1001.

SCHONFELD, T. & RUDGYARD, M. 1999 Steady and unsteady flows simulations using the hybrid flow solver avbp. *AIAA J.* **37**, 1378–1385.

SCHUMM, M., BERGER, E. & MONKEWITZ, P. A. 1994 Self-excited oscillations in the wake of two-dimensional bluff bodies and their control. *J. Fluid Mech.* **271**, 17–53.

SHANBHOGUE, S. J., HUSAIN, S. & LIEUWEN, T. 1997 Lean blowoff of bluff body stabilized flames: scaling and dynamics. *Prog. Energy Combust. Sci.* **333**, 375–402.

SHANBHOGUE, S. J., SANUSI, Y. S., TAAMALLAH, S., HABIB, M. A., MOKHEIMER, E. M. A. & GHONIEM, A. F. 2016 Flame macrostructures, combustion instability and extinction strain scaling in swirl-stabilized premixed CH_4/H_2 combustion. *Combust. Flame* **163**, 494–507.

SMITH, C., NICKOLAUS, D., LEACH, T., KIEL, B. & GARWICK, K. 2007 LES blowout analysis of premixed flow past V-gutter flameholder. In *45th AIAA Aerospace Sciences Meeting and Exhibit*, vol. 162. pp. 2007–170. AIAA.

SMITH, G. P., GOLDEN, D. M., FRENKLACH, M., MORIARTY, N. W., EITENEER, B., GOLDENBERG, M., BOWMAN, C. T., HANSON, R. K., SONG, S., GARDINER, W. C. JR *et al.* 1999 Gri-mech 3.0. *Tech. Rep.* University of Berkeley.

STOHR, M., BOXX, I., CARTER, C. D. & MEIER, W. 2012 Experimental study of vortex-flame interaction in a gas turbine model combustor. *Combust. Flame* **159**, 2638–2649.

TERHAAR, S., OBERLEITHNER, K. & PASCHEREIT, C. O. 2015 Key parameters governing the precessing vortex core in reacting flows: an experimental and analytical study. *Proc. Combust. Inst.* **35**, 3347–3354.

VAGELOPOULOS, C. M. & EGOLFOPOULOUS, F. N. 1994 Laminar flame speeds and extinction strain rates of mixtures of carbon monoxide with hydrogen, methane, and air. In *Symp. (Int.) on Combustion*, vol. 25, pp. 1317–1323. Elsevier.

VAREA, E., MODICA, V., VANDEL, A. & RENOU, B. 2012 Measurement of laminar burning velocity and markstein length relative to fresh gases using a new postprocessing procedure: application to laminar spherical flames for methane, ethanol and isooctane/air mixtures. *Combust. Flame* **159**, 577–590.

VIETS, H., PIATT, M. & BALL, M. 1981 Boundary layer control by unsteady vortex generation. *J. Wind Engng Ind. Aerodyn.* **7**, 135–144.

WICHMAN, I. S. & BRUNEAUX, G. 1995 Head-on quenching of a premixed flame by a cold wall. *Combust. Flame* **103**, 296–310.

WILLIAMS, F. A. 2000 Progress in knowledge of flamelet structure and extinction. *Prog. Energy Combust. Sci.* **24**, 657–682.

WILLIAMS, G., HOTTEL, H. & SCURLOCK, A. 1951 Flame stabilization and propagation in high velocity gas streams. *Proc. Combust. Inst.* **3**, 21–40.

WILLIAMS, G. C. & SHIPMAN, C. W. 1953 Some properties of rod stabilized flames of homogeneous gas mixtures. *Proc. Combust. Inst.* **4**, 733–742.

ZUKOSKI, E. E. & MARBLE, F. E. 1955 The role of wake transition in the process of flame stabilization on bluff bodies. In *Combustion Researches and Review*. Butterworths.

ZUKOSKI, E. E. & MARBLE, F. E. 1956 Experiments concerning the mechanism of flame blowoff from bluff bodies. In *Proceedings of the Gas Dynamics Symposium on Aerothermochemistry*, pp. 205–210. Northwestern University Press.